

RECENT ADVANCES IN MULTIPHASE FLOWS THROUGH POROUS AND FRACTURED MEDIA

G. Ahmadi*

Department of Mechanical and Aeronautical Engineering, Clarkson University
Potsdam, NY 13699-5725, USA

ABSTRACT

In this paper experimental and computational modeling methods for studying multiphase flows in porous and fractured media are studied. Particular attention was given to the flows in a laboratory-scale flow cell model. It is shown that the gas-liquid flows generate fractal interfaces and the viscous and capillary fingering phenomena are discussed. Experimental data concerning the displacement of two immiscible fluids in the lattice-like flow cell are presented. The flow pattern and the residual saturation of the displaced fluid during the displacement are discussed. Numerical simulations results of the experimental flow cell are also presented.

The numerical simulation results for single and multiphase flows through rock fractures are also presented. Fracture geometry studied was obtained from a series of CT scan of an actual fracture. Computational results show that the major losses occur in the regions with smallest apertures. An empirical expression for the fracture friction factor is also described. Applications to CO₂ sequestration in underground brine fields depleted oil reservoir stimulation are discussed.

Keywords: Multiphase flows, flow in porous media, fractured media, immiscible flows, computer model, reservoir engineering

1. INTRODUCTION

Underground sequestration of CO₂ in brine formations and stimulation of depleted oil and gas fields have attracted considerable attention in recent years. These require injecting gases into liquid saturated underground reservoirs on massive scale. The technology of injection of gas into liquid saturated porous media is only the latest of many that demand a better understanding of the fundamentals of multiphase flow through porous media. In particular, despite much research, viscous fingering at the interface of two immiscible fluids is not well understood. In addition, geological reservoirs are commonly composed of fractured rocks. The flow properties in rock fractures are poorly understood.

* Email-address of the corresponding author: ahmadi@clarkson.edu

In the present study, an experimental method for providing a fundamental understanding of fingering phenomena in geological sequestration is described. A “two-dimensional” flow cell of square-lattice networks is used in the setup as the porous media. Gas was injected at a constant rate into the flow cell, which was initially saturated with water. The entire displacement process was recorded until a stable state is reached. Image processing was used to provide the displacement flow pattern and gas saturation.

Two different modeling approaches were used to simulate gas displacements through networks that are similar to those of the physical experiment. These models consider a network grid structures with a rather simplified geometry. The first numerical model (is referred to as the network model) accounts for the effect of capillary pressure and viscous pressure drops in the network pores. The other numerical model was developed using the “volume-of-fluid” (VOF) of FLUENTTM code. The model solves the Navier-Stokes equation for both gas and the liquid phases. Here a grid of square cross-section flow channels with random widths and shape is generated, and the gas and liquid flows are numerically evaluated.

The results of the numerical models are compared with those obtained from the laboratory flow cell experiments. Particular attention is given to the fingering process, the effects of channel size distribution, and the evaluation of fractal dimension of the gas-liquid interface.

Flows through rock fractures are also studied. The computational model for the geometry of the fracture is constructed using CT scan of a real fracture. Sample simulated flow fields through the fractures are also presented. An empirical formula for friction factor for fracture flow is also discussed.

2. EXPERIMENTAL FLOW CELL

The main component of the experimental equipment is the flow cell, which was fabricated by sand blasting channels of random width into a glass plate, onto which a second, cover-glass plate was sealed. For the experiment reported in this paper, the size of the flow cell was 100mm×100mm, with an average channel depth of 0.3mm. The width of channels in the cell is uniformly distributed between 0.2mm-0.8mm. To study the flow patterns that occur when CO₂ is sequestered underground, the cell first is saturated with water, and then gas is injected until residual saturations of the two fluids are obtained. Different injection rates of displacing gas are used that lead to different capillary numbers. The mass of the displaced water, the pressure drop across the cell, and the flow pattern image are recorded at different times during each run. The diagram of the experimental setup is shown in Figure 1.

3. NETWORK MODEL

The network model of two-phase flow in porous media is intended to incorporate, as realistically as possible, the capillary pressure that tends to block the invasion of narrow throats and the viscous pressure drop in a flowing fluid. A two-dimensional porous medium

is modeled as a diamond lattice, consisting of pore-bodies of volume, ℓ^3 , at the lattice sites, connected by throats of length, ℓ , with a randomly chosen cross-sectional area between 0 and $b\ell^2$. This model is more general and perhaps more flexible than the other recently developed network models because both the throats and the pore-bodies have finite volume.

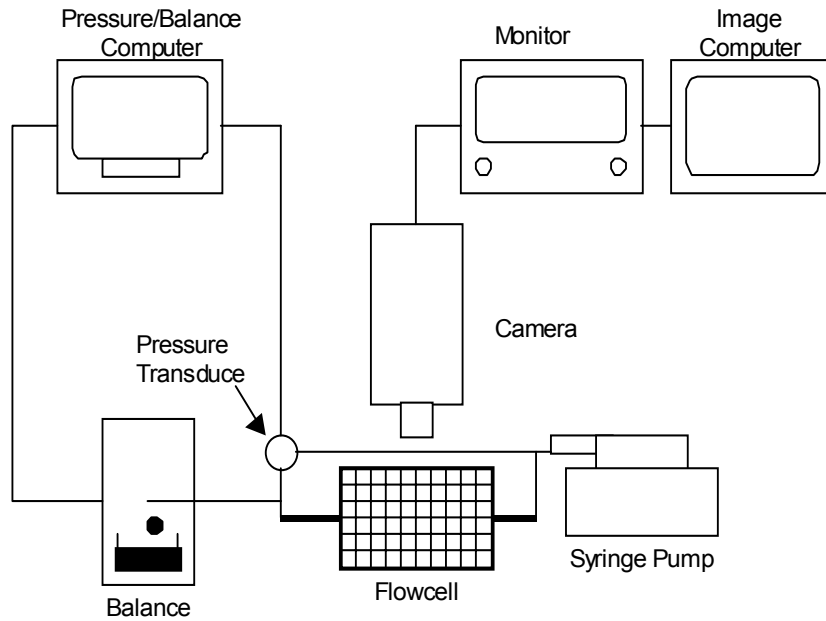


Figure 1. Experimental flow system

Throats in the model have elliptical cross-sections with a constant ratio, b , of the width of the ellipse to the height of the ellipse. This ratio is easily varied to incorporate both circular cross-sections used in many comparable models and more oblong throats found in these experimental models, such as those described in this paper. When an interface enters one of the throats, the pressure drop across the meniscus is fixed by contact angle, θ , the depth of the throat, h , and the surface tension, σ . That is

$$P_{\text{cap}} = \sigma \cos \theta \left(\frac{1}{h} + \frac{1}{bh} \right) \quad (1)$$

where bh is the width of the elliptical throat. The flow velocity is given by the throat conductance times the total pressure drop across the throat,

$$q = g_{\text{throat}} (P_{\text{nw}} - P_{\text{w}} - P_{\text{cap}}), \quad (2)$$

where P_{nw} and P_{w} are the pressures in the non-wetting and wetting fluids, respectively.

The transmissibility (conductance) of the throat is obtained by solving the Navier-Stokes

equation for steady state flow through a tube of constant elliptical cross-section. i.e.,

$$g_{\text{throat}} = \frac{bA_{\text{throat}}^2}{4\pi\mu_w\ell(b^2 + 1)(x + (1-x)M)}, \quad (3)$$

where A_{throat} is the cross-sectional area of the throat, x is the fraction of the throat of length ℓ which is filled with defending fluid, and $M = \mu_{\text{nw}}/\mu_w$, the ratio of the non-wetting, invading fluid's viscosity to that of the wetting, defending fluid. When $b=1$, Equation (3) reduces to the Poiseuille equation used for throats with circular cross-section. From Equation (2) it follows that the non-wetting fluid advances if the pressure difference between the pore filled with non-wetting fluid and the pore filled with wetting fluid exceeds the capillary pressure. Otherwise the non-wetting fluid will retreat.

Naive use of Equation (1) causes numerical difficulties because of the blocking that can occur if the non-wetting fluid is at the entrance to a throat, when the sum of the pressures found in Equation (2) is small. In such cases, a very small time step may be required. To solve this problem, we assume a sinusoidal increase in P_{cap} from zero at each throat inlet to the value in Equation (1) at the throat's center.

Volume conservation of the incompressible fluid dictates that the net volume flow, q , out of any pore-body, j , must be zero. Application of volume conservation to the situations at a particular pore leads to

$$\left(\sum_i g_i \right) P_j = \sum_i (g_i P_i) + \sum_i (f_i g_i P_i) \quad (4)$$

where the factor f is either zero, +1, or -1 if there is i) no meniscus in the throat, ii) the pore-body, j , is filled with non-wetting fluid and the connecting pore-body, i , is filled with wetting fluid, or iii) the pore-body is filled with wetting fluid and the connecting pore-body is filled with non-wetting fluid, respectively.

Once the location of the interface is known, the program iterates Equation (4), updating the pressure field until convergence is achieved to within a small residual. Then, the interface is advanced through a time chosen to be small enough to avoid spurious local oscillations without unnecessarily long program run-times. Having determined the interface and chosen the time step, we have attempted to make the flow rules as non-restrictive as possible. A full description of the network model and the model flow rules are given by Ferer et al. (2001).

4. VOLUME OF FLUID MODEL

The other numerical model uses a "volume of fluid" (VOF) method to describe the boundaries between two immiscible fluids in a porous media. Here the FLUENTTM code is used in the simulation. In this approach, a grid of square cross-section channels with random size and shape is generated to simulate the experimental flow cell. In the VOF

approach a single set of Navier-Stokes equation given as

$$\frac{\partial}{\partial t}(\rho u_j) + \frac{\partial}{\partial x_i}(\rho u_i u_j) = -\frac{\partial P}{\partial x_j} + \mu \frac{\partial}{\partial x_i} \left(\frac{\partial u_i}{\partial x_j} + \frac{\partial u_j}{\partial x_i} \right) + \rho g_j + F_j \quad (5)$$

is solved throughout the domain. In Equation (5), ρ is the averaged density of gas and water in cell, μ is the averaged viscosity, u_i is the velocity of gas and water in each grid, F_j is the source term, which accounted for the surface tension between the liquid and gas.

The volume fraction of gas and water is governed by the following continuity equation:

$$\frac{\partial \varepsilon_k}{\partial t} + u_j \frac{\partial \varepsilon_k}{\partial x_i} = 0 \quad (6)$$

where ε_k is the volume fraction of water or of air.

Interface between the liquid and gas is tracked by the volume fraction of water in the computational cell volume. In each grid, the slope of the gas-liquid surface is determined first, and then a line is constructed based on the fraction of water. A detailed description of the VOF method was given by Hirt and Nichols (1981).

The VOF analyses were performed for a variety of capillary pressures and capillary numbers and the results are compared with the experimental data.

5. FLOW CELL RESULTS

This section presents the results and analysis of the flow patterns during the constant injection experiment in the flow cell. Comparison between the experimental flow patterns and that of numerical simulations is also presented. In addition, the variation of the measured residual saturation under various conditions is discussed.

In the experiment, two types of flow patterns were observed during the displacement of two immiscible fluids: i) capillary fingering, which was dominated by capillary pressure in the random network of throats and occurs at a very low capillary number; and ii) viscous fingering, which was dominated by the gas viscosity and occurs at high capillary numbers. Figure 2 shows typical capillary fingering and viscous fingering recorded in the experiment. The capillary fingering shown in Figure 2(a) occurs when the capillary number is 7.36×10^{-7} . It is seen that as the gas penetrates into the flow cell, it formed fingers, which reconnect and trap clusters of liquid (water). The size of the water clusters varies from the width of the channel to the order of the flow cell size. Figure 2(b) shows a viscous fingering flow pattern for a capillary number of 3.25×10^{-5} . In this figure, the gas fingers grow in a branching, dendritic pattern with much fewer clusters of trapped water.

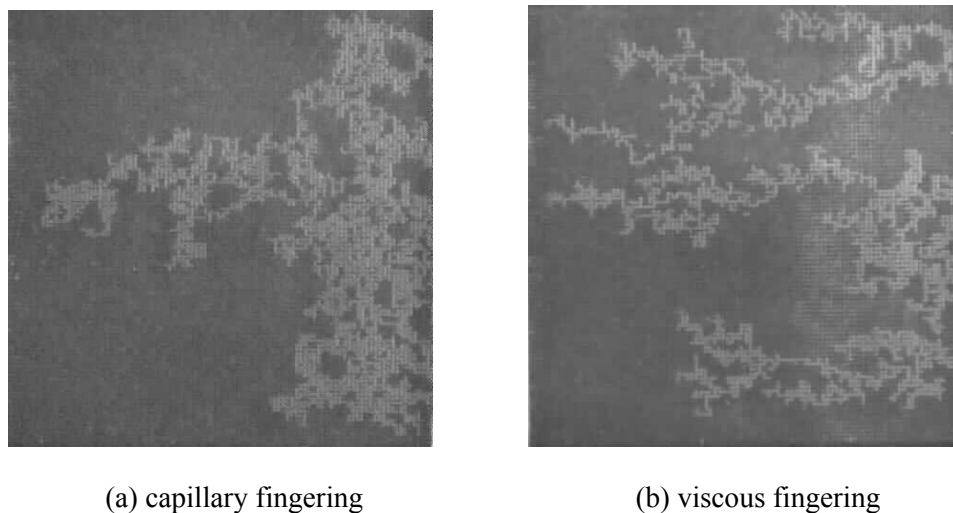


Figure 2. Flow patterns observed in the experiment for different capillary numbers.

Figure 3 shows infiltration patterns from the network model that correspond to both viscous and capillary fingering types. Figure 3(a) is for a very low velocity and thus low capillary number flow. It exhibits capillary fingering similar to that of Figure 2(a), with many clusters of trapped water cells behind the interface. Figure 3(b) was simulated at a much higher velocity and thus at a high capillary number. This figure shows long branching fingers and few clusters of trapped water, similar to Figure 2(b), which is the characteristic of viscous fingering.

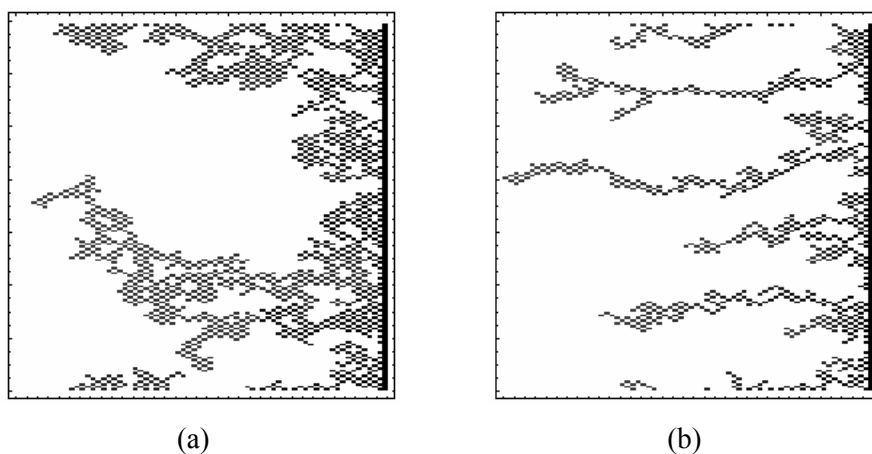


Figure 3. Infiltration patterns of capillary and viscous fingering from the network model.

Flow structures from the VOF model is shown in Figure 4. For a low gas injection velocity, Figure 4(a) presents a flow pattern similar to those of Figure 2(a) and 3(a). As the gas injection velocity increased to a much higher value, the flow pattern developed from

reconnect-trap-water-clusters to dendritic fingers, which is similar to those of Figures 2(b) and 3(b).



Figure 4. Flow patterns obtained from volume of Fluid model with different injection flow rates

In some instances, flow patterns occurring during the displacement of two immiscible fluids have been shown to have fractal characteristics (Feder, 1988). Our findings are consistent with these observations. In this study, a box counting method is used to obtain the relationship between the number of boxes containing gas, which is denoted as N , and the widths of each box, referred to as L . Figure 6(a) presents the results in logarithmic scale, which indicates that N has a power law relationship with L given as

$$N=L^{-\alpha}, \quad (7)$$

where α is the fractal dimension.

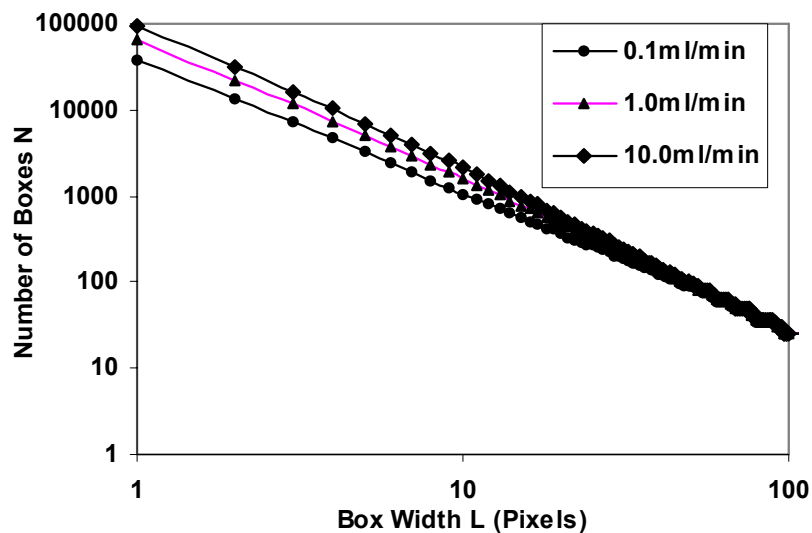


Figure 5. Box counting results of experimental data.

Figure 6(a) presents the variation of the fractal dimension with capillary numbers. It is observed that the experimentally measured fractal dimension increases from 1.6 to 1.85 with capillary number. This results is consistent with the fractal dimensions of Invasion Percolation and DLA are reported to be in the range of 1.7-1.9 (Ferer, 1991). Note that the Invasion Percolation (IP) model is a quasi-static model based on the assumption that at each time step the displaced fluid invades the interfacial channel with the lowest capillary pressure. IP is a good method of modeling the process of pure capillary fingering. The diffusion-limited aggregation (DLA) model, which is based on the random walk of particles through a network, has been shown to be an effective model for viscous fingering process.

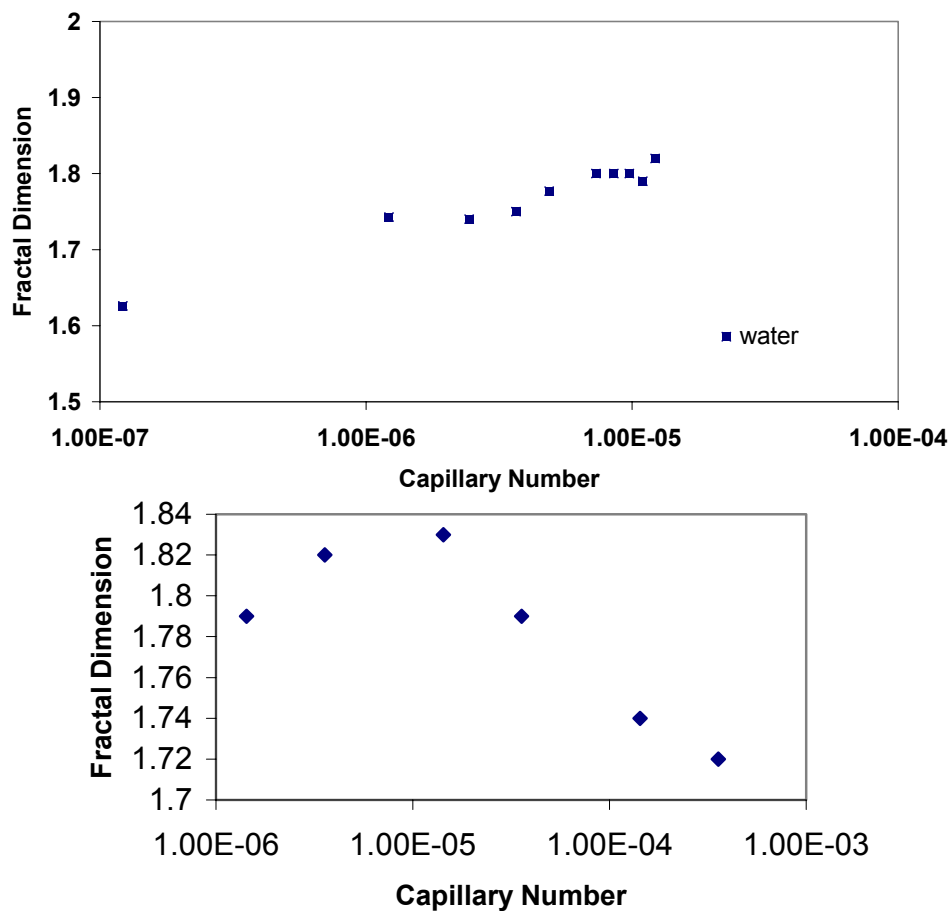


Figure 6. Fractal Dimensions obtained from experimental data and network models for different capillary numbers

An alternative technique is used for evaluating the fractal dimension of the network flow model shown and the results are shown in Figure 6(b). This approach is based on the relationship between average position of the interface and time. For steady and stable flows, the position of the interface is a linear function of time. However, in cases of viscous and capillary fingering, the mean position of the interface exhibits a power law relationship with

time given as

$$\langle x \rangle = ct^{1/(D_f-1)} \quad (8)$$

where $\langle x \rangle$ is average position of the infiltrating fluid, t is time, c is some constant, and D_f is the fractal dimension. Figure 6(b) shows a plot of fractal dimension versus capillary number for the network model results. Here the fractal dimension varies between 1.65 and 1.85 that are consistent with the range obtained in the experiment and with theoretical results of DLA and IP models.

Figure 7 shows the variation of the gas saturation at the stable state and break through point with capillary number. During the process of displacement, the gas penetrates the flow cell from the inlet manifold, the break through point refers to the moment that the first branch of gas reaches the outlet manifold of the flow cell, while the stable state indicates the situation that the gas saturation and gas flow pattern do not vary with time any more. It is seen that as the capillary number increases from 10^{-8} to 10^{-3} , which corresponds to the variation of gas injection flow rate from 5 $\mu\text{l}/\text{min}$ to 100 ml/min , the stable gas saturation first decreases slightly to a minimum value, and then increases with the capillary number. However, as the stable gas saturation increases with capillary number, the gas saturation at the break through point keeps constant. The transition of the flow pattern from capillary fingering to viscous fingering can account for the decrease in the stable gas saturation at a very small capillary number, which needs to be proven with additional experimental data. A linear increase in the stable gas saturation at a large capillary number indicates that the stable gas saturation is proportional to the gas injection flow rate in a certain range.

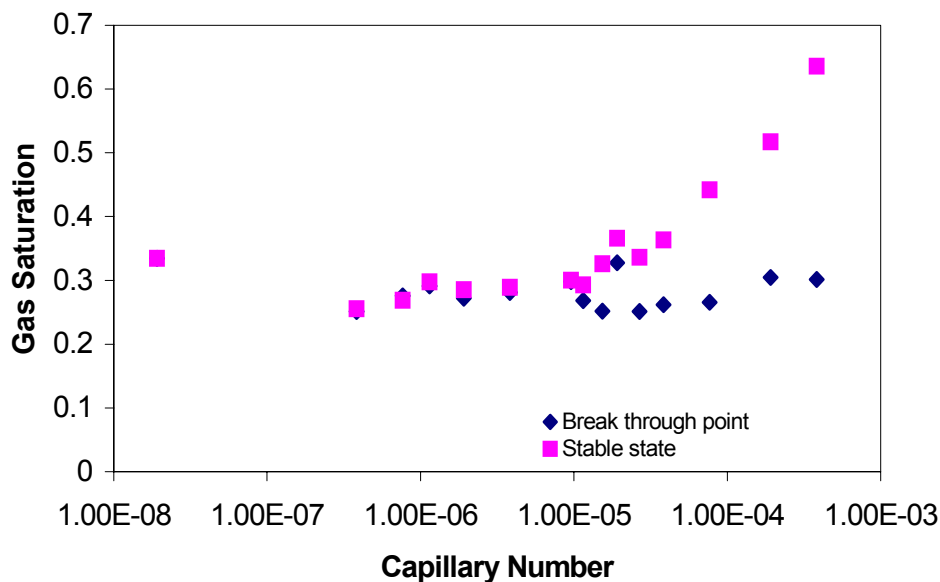


Figure 7. Gas saturation at the stable state and break through point with different capillary numbers.

To compare the experiment results with that of the network model, Figure 8 shows the average position $\langle x \rangle$ of the infiltrating gas with time in a logarithmic scale. Here the $\langle x \rangle$ is the first moment of mass, which is defined as (Ferer, 1991)

$$\langle x \rangle = \frac{\int x S(x, t) dx}{\int S(x, t) dx} \quad (9)$$

It is seen that for different gas injection flow rates, $\langle x \rangle$ increases with time until it reaches a constant. According to Equation (8), the fraction dimension D_f calculated from Figure 8 varies from 1.69 to 1.75, which corresponds to the results in Figure 6.

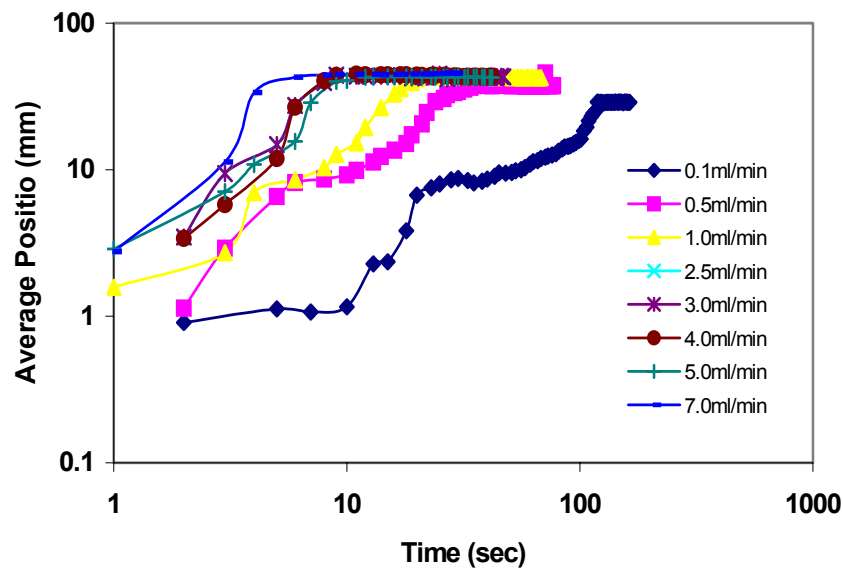


Figure 8. Time variation of average position with different gas injection flow rates.

5. FRACTURE FLOW ANALYSIS RESULTS

Four sections of the fracture that are analyzed in this study are shown in Figure 2. The length of the fracture is 10 cm and the fracture aperture varies from a minimum of 240 μm to a maximum of 1.5 mm. There are also very few regions with larger height and there are several areas where the fracture is closed. In the sections shown in Figure 2, which are selected for flow analysis, the minimum height is 240 μm . These sections do not have completely obstructed regions and are selected so that the two-dimensional flow simulation could be performed.

For a range of flow rates (per unit width) from $0.03 \text{ mm}^2/\text{s}$ to $3 \text{ mm}^2/\text{s}$, flows in various fracture sections are simulated. Computational grids of 15,000 to 17,000 cells are generated using GAMBIT™ preprocessor for different fracture sections. FLUENT™ code is used for the flow simulation analysis. Single-phase flows of air are studied. For air, a density of 1.225 kg/m^3 and a viscosity of $1.8 \times 10^{-5} \text{ kg/m.s}$ are assumed.

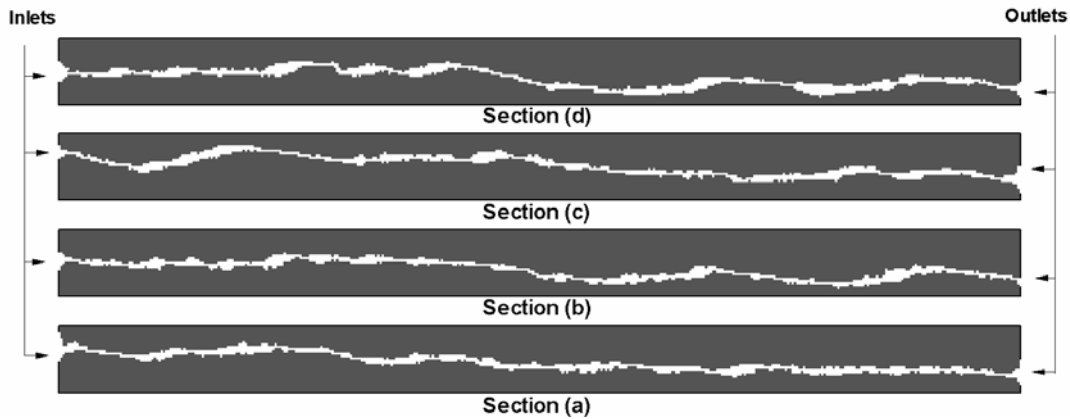


Figure 9. Several sections of the induced fracture

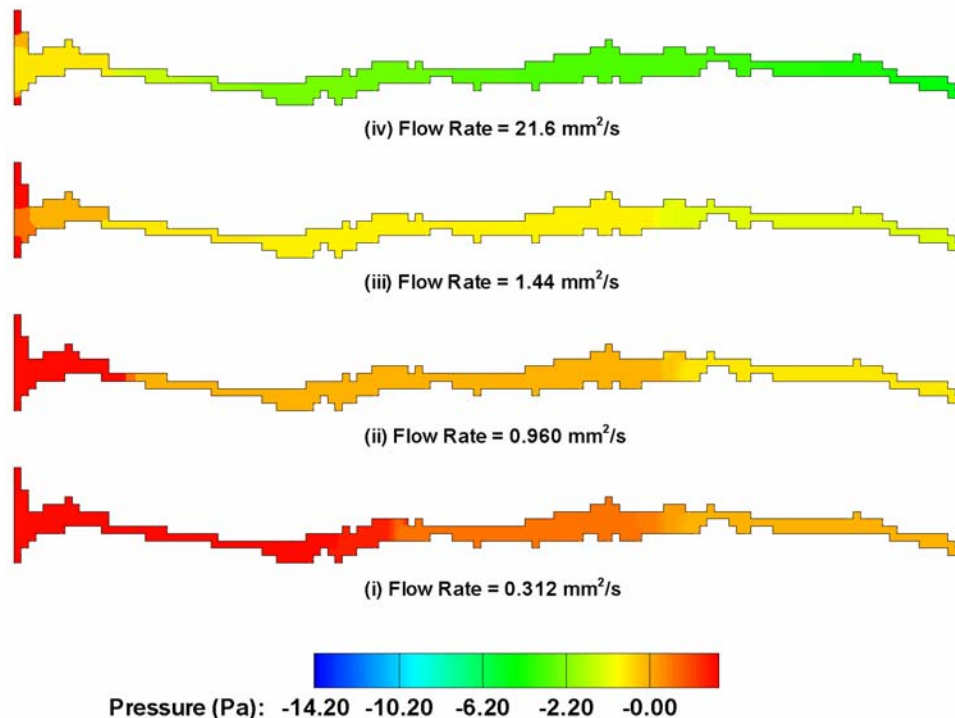


Figure 10. Pressure contours across section (a) of the fracture for various flow rates for airflow

Figure 10 shows the contour plot for variations of static pressure in fracture section (a) for several airflow rates in the range of $0.03 \text{ mm}^2/\text{s}$ to $3 \text{ mm}^2/\text{s}$. This figure shows a roughly linear variation of the pressure along the fracture. The results for fracture sections (b)-(d) are qualitatively similar to the one shown in Figure 10 and therefore are not shown here. It is seen that the amount of pressure drop increases in direct proportion to the flow rate.

The velocity vector fields for airflow in section (a) and for a flow rate of $21.6 \text{ mm}^2/\text{s}$ is plotted in Figure 11, where the computational grid is also shown. It is seen that the flow is channeled into one main high-speed stream with many dead zones of very low velocities. The maximum velocity is about 16 cm/s for airflow.

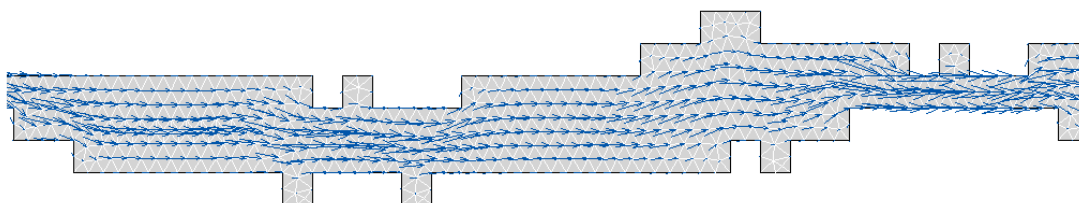


Figure 11. Velocity vectors and the grid schematics in a segment of fracture section (a) for flow rate of $21.6 \text{ mm}^2/\text{s}$ for air

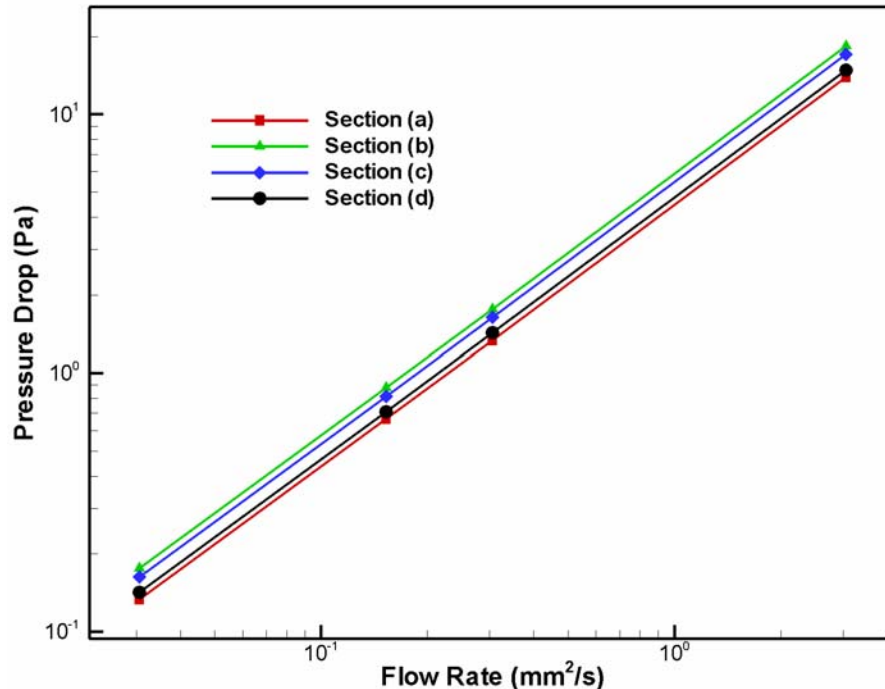


Figure 12. Computed variation of pressure-drop with fracture flow rate for different sections for airflow

The computed variations of pressure drop across the fracture for sections (a)-(d) for a range of flow rates for air are shown in Figure 12. The pressure drop varies from 0.01 to 20 Pa when the flow rate changes from 0.03 mm²/s to 3 mm²/s (Reynolds numbers varies from 0.002 to 0.209). It is seen that the pressure drop increases linearly with the flow rate for all four sections. While the pressure drop values are comparable, the highest pressure drop occurs in section (b), the lowest in section (a), and order in different sections are given as, $\Delta P_b > \Delta P_c > \Delta P_d > \Delta P_a$.

Additional simulation results show that the highest pressure drops occur in regions with lowest aperture, and the smallest aperture regions are responsible for more than 60% to 70% of the fracture pressure drops. Based on the simulation results for a wide range of flow rates, a semi-empirical expression for the friction coefficient was derived. That is,

$$f = \frac{144}{Re_{\bar{H}}} \left(1 + 0.25 Re_{\bar{H}}^{0.687} \right), \quad Re_{\bar{H}} \leq 100. \quad (10)$$

Where \bar{H} is the mean minus one standard deviation of the aperture height, and the Reynolds number is given as,

$$Re_{\bar{H}} = \frac{Q}{v} \quad (11)$$

Equation (10) preserves the inverse dependence of the friction factor with the Re at small Reynolds numbers and has the conventional nonlinear dependence on Re due to laminar inertial effects at higher Reynolds numbers.

7. CONCLUSIONS

Experimental and computational studies of displacement of immiscible fluids in a flow cell are performed. Sample computational results for flow through rock fractures are also presented. The flow patterns during the displacement are analyzed. On the basis of results presented, the following conclusions are drawn:

- For the flow cell, as the capillary number increases, stable saturation of the displacing fluid first decreases when the capillary number is small, then increases with further increase of the capillary number.
- For the flow cell, the break through saturation does not vary appreciably with the increase of the capillary number.
- Fractal dimension of the flow pattern at stable state increases with the capillary number.
- For the fracture, the bulk of the flow paths through the central channel.
- Major fraction of the pressure drop occurs in the region with smallest aperture.
- Friction factor for the fracture may be used for pressure drop evaluation.

REFERENCES

1. Ferer, M., Grant S. Bromhal, and Duane H. Smith., Pore-Level Modeling of Immiscible Drainage: Validation in the Invasion Percolation and DLA Limits, submitted to *Water Resources Research*, 2001.
2. Hirt, C.W., Nichols, B.D., Volume of Fluid (VOF) Method for the Dynamics of Free Boundaries, *Journal of Computational Physics*, **39**(1981) 201-225.
3. Feder, J., *Fractals*, Plenum, New York, 1988.
4. Ferer, M., Sams, W.N., Geisbrecht, R.A. and Smith, D.H., Scaling of Fractal Flow, *Physica*, 1991, pp. 273-280.
5. Fluent Corp, Users' Guide of FLUENT Version 4.5, 1999.
6. Meakin, P., *Fractals, scaling and growth far from equilibrium*. Cambridge University Press, Cambridge, 1998.